Continental slope-confined canyons in the Pearl River Mouth Basin in the South China Sea dominated by erosion, 2004–2018

Shaoru Yin [a, b], Lin Lin [c], Ed L. Pope [d], Jiabiao Li [a, b *], Weifeng Ding [a, b], Ziyin Wu[a, b *], Weiwei Ding[a, b], Jinyao Gao [a, b *], Dineng Zhao[a, b]

[a] Key Laboratory of Submarine Geosciences, State Oceanic Administration, Hangzhou 310012, China

[b] Second Institute of Oceanography, Ministry of Natural Resources, Hangzhou 310012, China

[c] Guangzhou Marine Geological Survey, Guangzhou 510075, China

[d] Department of Geography, Durham University, Science Laboratories, South Road, Durham, DH1 3LE, United Kingdom

E-mail: shaoru2017@outlook.com; linlin_gmgs@163.com; edward.pope@durham.ac.uk; jbli@sio.org.cn; fwxf1769@126.com; zywu@vip.163.com; wwding@sio.org.cn; jygao@mail.hz.zj.cn; zhaodineng@sio.org.cn.

* Corresponding author

Abstract

Repeat multibeam bathymetric surveys conducted in 2004, 2005 and 2018 show that seven slope-confined canyons on the continental slope of the Pearl River Mouth Basin, South China Sea, were dominated by large volume, widespread erosion. Erosion volumes were up to 3.4 times greater than deposition volumes. Erosion-dominated areas of the canyons are up to 2.3 times greater than areas dominated by deposition. Average rates of erosion (ranging from 0.7 to 0.8 m/yr) were greater than average rates of deposition (ranging from 0.5 to 0.8 m/yr). In plan view, the erosion-dominated zones exhibit two characteristic shapes: (1) linear, found mainly in upper canyon reaches, distributed predominantly along canyon axes and at the base of eastern canyon walls, and; (2) blocky, found mainly in lower canyon reaches, widely distributed along the steep canyon walls and on lower-canyon interfluves. The deposition-dominated zones are scattered along canyon floors and walls. Seismic reflection data show lateral shifts of canyon fill deposits through time, indicative of longer-term eastward canyon migration. The linear erosion-dominated zones may be attributed to erosive turbidity currents triggered by energetic internal solitary waves shoaling on the shelf. The eastward canyon shifts were likely induced by rapid near-bed eastward currents generated mainly by westward propagating powerful internal solitary waves of depression. The widespread erosion in the deeper canyon areas and interfluves is likely a consequence of slope instabilities associated with the presence of gas hydrates. This study indicates that active sedimentary processes can occur in slope-confined canyons

even during sea level highstands. Local, site-specific oceanographic and geological features (e.g., internal solitary waves, gas hydrates) can significantly increase sedimentary activity in and around submarine canyons.

Keywords: submarine canyons; sedimentary processes; turbidity currents; South China Sea

1. Introduction

Submarine canyons are the largest morphological features shaping present continental margins (Reading and Richards, 1994). These features not only convey large volumes of sediment from the continental shelf to the deep sea (Shepard and Dill, 1966; Shepard, 1981; Normark and Carlson, 2003; Wynn et al., 2007), they also sort the transported sediments (Posamentier and Walker, 2006). Coarser (sandy) canyon-sorted sediments are important potential hydrocarbon reservoirs (Deptuck et al., 2003; Posamentier and Kolla, 2003).

Turbidity currents are the dominant mechanism by which sediment is transported within submarine canyons. The magnitude and frequency of these flows has been argued to fluctuate as a consequence of sea level change (Posamentier and Walker, 2006; Covault and Graham, 2010). Powerful and frequent turbidity currents have been suggested to occur during sea level lowstands due to the basinward migration of fluvial systems and enhanced sediment supply to continental slope and basin floor (Vail et al., 1977; Burgess and Hovius, 1998). However, recent studies have demonstrated that

strong and frequent turbidity currents also occur in submarine canyons during sea level highstands, thus allowing for the maintenance of canyon morphology (e.g., Shepard, 1981; Pratson et al., 1994; Smith et al., 2005; Mulder et al., 2012; Mountjoy et al., 2018). Frequent turbidity current occurrence during highstand conditions has been suggested by recent observations in Monterey Canyon (Paull et al., 2003, 2018; Xu et al., 2004), Var Canyon (Khripounoff et al., 2009), Congo Canyon (Azpiroz-Zabala et al., 2017), and Gaoping Canyon (Zhang et al., 2018). Notably, these observations are limited to shelf-incised submarine canyons. No observations of turbidity currents in slope-confined canyons, accounting for 69% of the large canyons on Earth (Harris and Whiteway, 2011), have yet been reported.

The Pearl River Mouth Basin, South China Sea (Fig. 1), is one of the two most important gas hydrate drilling areas (i.e., Shenhu area, Yang et al., 2015) in the South China Sea. Here, 19 submarine canyons are confined on the upper continental slope (Zhu et al., 2010; Gong et al., 2013; He et al., 2014; Zhou et al., 2015). These canyons face the Pearl River, the second largest river draining into the South China Sea (Wang and Li, 2009). These slope-confined canyons are located in an area that is notable for the occurrence of vigorous oceanographic processes, including quasi-steady water exchange with the Pacific (Wang and Li, 2009) and some of the world's largest internal solitary waves (Alford et al., 2015). The complex and special hydrodynamic environment makes the modern canyons in the Pearl River Mouth Basin an ideal site for addressing the research gap on sedimentary processes in slope-confined canyons

during sea level highstands. In addition, understanding the contemporary activity of such canyons can help assess geohazards relevant to ongoing gas hydrate exploitation in the area.

In this paper, building on published work that has focused on long-term (i.e., the middle Miocene to present) (Zhu et al., 2010; Gong et al., 2013; Zhou et al., 2015) development of the canyons on the continental slope of the northern South China Sea, this study addresses contemporary canyon processes within seven slope-confined canyons. Based on repeat multibeam bathymetric surveys conducted in 2004, 2005, and 2018, as well as two canyon-crossing multichannel seismic reflection profiles, our work (1) illustrates bathymetric changes between 2004 and 2018 in the upper canyon reaches, as well as between 2005 and 2018 in the lower canyon reaches; (2) documents the distribution, sediment volumes, and rates of erosional and depositional activity; (3) discusses mechanisms possibly responsible for sedimentary processes in the slope-confined canyons and; (4) compares the sedimentary processes of these slope-confined canyons with those of shelf-incised canyons on other continental margins.

2. Geological setting

The South China Sea is one of the largest marginal seas in the western Pacific region. The modern oceanic basin formed as a result of crustal rifting and subsequent drifting during the late Eocene or early Oligocene to middle Miocene (Taylor and Hayes 1980; Li et al. 2014). Subsequent to the late Miocene, as the South China Sea basin

entered a phase of regional thermal subsidence, its northern and southern passive continental margins gradually formed.

The study site, is located on the continental slope of northern South China Sea, southeast of Hong Kong and the mouth of the Pearl River (Fig. 1A). This area structurally lies in the Pearl River Mouth Basin (Fig. 1A), one of the largest oil- and gas-bearing basins offshore from China. The study area covers about 1647 km^2, with water depths between 200 and 1600 m. The regional slope is approximately 1.6° on average (He et al., 2014). The 19 slope-confined canyons (Fig. 1B) are the most prominent morphologic features. Drilling results suggest that the late Miocene to Pleistocene canyon deposits in the study area are dominated by deep-water mud and silty mud, intercalated with sandy layers (Lüdmann et al., 2001; Gao et al., 2012). The muddy layers are mostly distributed in the inter-canyon areas, and the sandy layers occur mostly in the canyon fills. Content of clay minerals in the inter-canyon area sediments may up to 64% on average (Gao et al., 2012).

The main sediment source within the study area is the Pearl River (Fig. 1). Since 1980, the Pearl River has annually discharged approximately 300×10^9 m^3 of water (Gu et al., 1990) and $20–30\times10^6$ tons of sediment into its estuary (Wu et al., 2018). At the river mouth, the Pearl River delta has prograded at an average rate of 17 m/yr over the past 6,000 years (Huang and Song, 1981; Fyfe et al., 1999). The present Pearl River delta is confined within the estuary of the river (Wei and Wu, 2011; Wu et al., 2014).

Seventeen of the 19 submarine canyons on the continental slope of the Pearl River

Mouth Basin, were first documented by Zhu et al. (2010). These 17 canyons, which are found at water depths between 450 and 1500 m, are 30–60 km long, 1.0–5.7 km wide, and 50–300 m deep (Zhu et al., 2010). The canyons have been migrating northeastward since the middle Miocene (Zhu et al., 2010; Gong et al., 2013; Zhou et al., 2015). The evolution of the canyons includes three stages: the early lowstand incision stage, the late lowstand lateral-migration and active-fill stage and, the transgression stage when Pearl River no longer directly delivered sediment to the canyons (Gong et al., 2013).

Submarine landslides on the flanks of the 19 canyons were investigated by He et al. (2014). A total of 77 landslides characterized by small area (0.53–18.09 km^2 in the plan view) and short run-out distances (<3.5 km) were identified in the canyon area. Seafloor undulations are found in the canyon head areas and lower reaches, with some of the undulations linking to slope instabilities (Qiao et al., 2015). The seven canyons in the study area correspond to C5 through C11 labeled by Zhu et al., 2010, C6 through C12 labeled by He et al. (2014) which we adapt in this study (Fig. 1B). Among the seven canyons, C6 through C9 correspond to C4 through C1 in Gong et al. (2013), respectively.

3. Material and methods

3.1.Bathymetric surveys

Three repeat multibeam bathymetric data surveys and two multichannel seismic reflection profiles are used in this study. The first bathymetric survey (Fig. 1B),

covering the upper canyon reaches, was collected in 2004, using an ELAC Bottom Chart 1180/1050 multibeam system. The second bathymetric survey (Fig. 1B), covering the lower canyon reaches, was collected in 2005, using a RESON SeaBat 8150 multibeam system. The third bathymetric survey, covering the entire canyon region, was collected in 2018, using a Kongsberg Maritime EM 122 multibeam system.

The three original multibeam soundings were processed using CARIS HIPS and SIPS software (Caris HIPS and SIPS, version 8.1.9). This processing included sound velocity profile corrections, tidal level correction, editing navigation data and altitude data (Zhao et al., 2015), followed by a work flow using Combined Uncertainty and Bathymetry Estimator (CUBE) and "Surface filter" to eliminate outliers in the raw data (Calder and Mayer, 2003; Zhao et al., 2019). The swath angle surface method in CARIS HIPS and SIPS software was used to build the high-resolution seabed digital terrain model (DTM) with a grid resolution of 200 m.

Subtraction of the repeat mapping surfaces was used to document changes in seafloor elevation between 2004 and 2018 in the upper canyon reaches, as well as between 2005 and 2018 in the lower canyon reaches. Artifacts in the multibeam bathymetric data are identified mainly based on two features: regionally linear abnormal bathymetry; isolated abnormal bathymetry, especially on the survey boundaries.

Changes in elevation between the different datasets were used to identify areas of erosion (negative change) and deposition (positive changes). From this we were able to

calculate volumes of eroded and deposited sediment, the relative proportion of erosion-dominated and deposition-dominated areas within the canyons, and the rates of erosion and deposition during the 14 years.

3.1.1. Elevation difference correction

To quantify whether any corrections were necessary between the different surveys, we analysed whether there were any systematic differences between surveys in selected references areas. The reference areas were selected on the basis that they should be outside in influence of any sediment density flows than may occur and thus any changes are likely to be a consequence of difference between the survey instruments (Wright et al., 2008; Le Friant et al., 2010). Two reference areas (Z1 and Z2, Fig. 4) were selected above the canyons to analyse the comparability of the 2004 and 2018 surveys. Two references areas (Z3 and Z4, Fig. 4) were selected significantly below the canyons to analyse the comparability of the 2005 and 2018 surveys. The mean value of difference in depths for the Z1 – Z4 was -3.1 m, -3.6 m, -5 m and -5.1 m, respectively. As a consequence of these systematic difference, a 3 m and 5 m correction to the observed elevation differences was applied to the 2004 – 2018 and 2005 – 2018 surveys, respectively.

3.1.2. Accounting for uncertainty

Accounting for possible errors is necessary when using repeat multibeam sonar surveys to assess seabed change and is often overlooked (Schimel et al. 2015). Sources of error can include differences in the sonar system used, vessel configurations, vessel motion,

tide, parameters affecting sound velocity and absorption, low signal-to-noise ratios and bottom detection algorithms (Hare et al., 1995; Lurton, 2003; Lurton and Augustin, 2010). To assess uncertainties in our elevation change data, we used the fixed reference uncertainty method described by Schimel et al. (2015). This was achieved by selecting two areas as reference areas for the 2004-2018 surveys (upper canyons) and 2005-2018 surveys (lower canyons). The reference areas (Z1 and Z2 in upper canyons, and Z3 and Z4 in lower canyons, Fig. 4), were assumed to stay unchanged between surveys. The standard deviation of the elevation differences in each reference area (1.2 m, 1.6 m, 2.5 m, 1.9 m for Z1–Z4, respectively) is treated as a possible error in derived erosion (deposition) thickness, and thus as the detectable threshold in elevation change (Wright et al., 2008; Le Friant et al., 2010). The thresholds of elevation change between the 2004 and 2018 surveys and the 2005 and 2018 surveys are 1.5 m and 2.5 m, respectively. This equates to a volumetric uncertainty in each grid cell of 6×10^4 m^3 and 10×10^4 m^3 respectively.

3.2.Seismic data

The two multichannel seismic reflection profiles, collected in 2006, have a domain frequency between 72 and 96 Hz in the near-seafloor interval, which gives a vertical resolution (tuning thickness) of about 4 to 6 m (assuming an average interval velocity of about 1700 m/s, as estimated from well-logging data in Gao et al., 2012). Each seismic profile is about 25 km long. The seismic profiles were used to identify subsurface features in the study area.

4. Results

4.1 General morphology

Two significant morphologic features were identified in the study area, based on the bathymetric data: submarine canyons and scarps.

Seven submarine canyons (canyons C6 through C12) are present on the upper continental slope of the study area (Figs. 1B and 2). The canyon heads are located approximately 300 km southeast of the Pearl River mouth and 1 to 5 km beyond the shelf edge. These canyons (Tab. 1) extend downslope from approximately 700 m water depth (range = 538 to 865 m) to approximately 1500 m water depth (range = 1405 to 1663 m). Average canyon dimensions are approximately 33 km long (range = 23 to 40 km) and about 3 km wide (range = 1.1 to 4.8 km). The canyon heads are the narrowest canyon sections. The slope gradients of the canyon axes commonly decrease downslope, from approximately 4° at the canyon heads (range = 2.9° to 4.9°) to approximately 1.0° at the canyon mouths (range = 0.8° to 1.0°). Some canyons (C6, C9, C10, and C11) include a steep mid-canyon section. All seven canyons have steep sidewalls, with slopes of 3° to 14°. The eastern walls are usually steeper than the western ones (Fig. 2A).

Numerous slope scarps are present on the ridges between the canyons (Fig. 2). These scarps are crescent-shaped, and most are found at water depths ranging from 1000 to 1600 m. Additional scarps occur on the seafloor close to the canyon heads. These scarps are up to 5 km long, with headwall vertical relief of up to 68 m and

headwall gradients of 4° to 9°.

4.2 Canyon-related seismic facies

Three significant seismic facies were identified in the study area, based on the seismic reflection data: channel fill, contorted, and transparent to chaotic facies.

Channel fill seismic facies are characterized mainly by chaotic or transparent seismic reflectors, with fill boundaries defined by high-amplitude reflection interfaces (Fig. 3). The chaotic configurations are usually characterized by high-amplitude reflectors, whereas the transparent configurations are commonly characterized by low-amplitude reflectors. In cross-section, the canyon fills are relatively narrower (approximately 0.5 km) in the upper reaches and wider (approximately 1.5 km) in the lower reaches. These fills show evidence of eastward canyon migration in both the upper and lower reaches (Zhu et al., 2010; Gong et al., 2013).

Contorted seismic facies are characterized by contorted or steeply dipping reflectors (Fig. 3). These features are distributed mainly along the interfluves of the lower canyon reaches and hanging on the canyon walls. Normal faults often appear in the contorted seismic facies (Fig. 3). It is noted that the contorted reflections usually show increasing fold amplitude or wave relief with depth (Fig. 3C). The most significant modern morphologic expressions of the contorted seismic facies are the abundant slope scarps (Fig. 2).

Transparent to chaotic seismic facies are characterized by transparent reflectors

capped by high-amplitude chaotic reflectors (Fig. 3C, D). These features, which exhibit a vertical columnar or cone shape, are found beneath the interfluves of the lower canyon reaches.

4.3 Elevation change

Comparison of the 2004 and 2018, and the 2005 and 2018 bathymetric surveys shows significant elevation changes in the upper canyon reaches and in the lower reaches between surveys (Fig. 4). Both negative (erosion) and positive (deposition) changes in elevation are recorded.

4.3.1 Erosion

In terms of areal coverage, the erosion-dominated zones (negative elevation change) occupy ~44 % (canyon C9) to ~56 % (canyon C8) of each individual canyon (Tab. 2; Fig. 5A). The canyon-specific volume of eroded sediment (Tab. 2, Fig. 5B) ranges from about 32×10^6 m^3 (canyon C8) to 183×10^6 m^3 (canyon C10) in each upper canyon reach (2004–2018), and from about 297×10^6 m^3 (canyon C9) to 506×10^6 m^3 (canyon C10) in each lower canyon reach (2005–2018). The erosion rate in each canyon ranges from 31×10^6 m^3/yr (canyon C8) to 52×10^6 m^3/yr (canyon C10) (Fig. 5B). The average erosion thickness is 7–11 m in each upper canyon reach and 9.5–12.5 m in each lower canyon reach. The average vertical erosion rate (in thickness) in each canyon ranges from about 0.7 m/yr to 0.8 m/yr (Fig. 5C).

The zones dominated by erosion have two characteristic shapes: linear and blocky

(Fig. 4). The linear zones occur mainly in the upper reaches at water depths shallower than ~1000 m (i.e., within 8 km downstream of the canyon heads), along the canyon axes and at the base of the eastern canyon walls (Figs. 4 and 6). The linear zones range in width from 0.5 to 1.0 km. In contrast, the blocky zones occur mostly in the lower reaches at water depths greater than ~1000 m, though a few do occur in the upper reaches. These zones appear on canyon sidewalls, usually linked to those on the submarine canyon interfluves (Figs. 4 and 6). The blocky zones range in length from 0.5 to 5.0 km and in width from 0.2 to 2.0 km. The area of each irregularly shaped zone dominated by erosion is about 1 km^2 on average. Along- and cross-slope profiles of elevation change show eastward canyon migration during the past 14 years, which is more significant in the upper reach (Fig. 6).

4.3.2 Deposition

The deposition-dominated zones (positive elevation change) occupy ~22 % (canyon C12) to 45 % (canyon C6) of each individual canyon's area (Tab. 2; Fig. 5A). This is much less extensive than the area dominated by erosion (Fig. 5A). The canyon-specific volume of sediment deposition (Tab. 2) ranged from ~72×10^6 m^3 (canyon C8) to 202×10^6 m^3 (canyon C9) in each upper canyon reach (2004–2018), and from ~70 $\times10^6$ m^3 (canyon C8) to 226×10^6 m^3 (canyon C7) in each lower canyon reach (2005–2018). The rate of deposition in each canyon ranges from 10.7×10^6 m^3/yr (canyon C8) to 28×10^6 m^3/yr (canyon C7), which is only 30–80 % of the erosion rate in each canyon. The average thickness of deposited material is ~7–10 m in the upper canyon reaches,

and 6–14 m in the lower canyon reaches. Average deposition rate in each canyon ranges from about 0.5 m/yr to 0.8 m/yr (Fig. 5C).

The deposition-dominated zones, like the erosion-dominated zones, exhibit both linear and blocky shapes. Only a few are linear, with a length up to 2.4 km (canyon C10) and widths ranging from 172 to 353 m. The largest one has an area of 0.5 km^2 (canyon C10). These linear features extend along the base of some of the canyon walls. Most of the deposition-dominated zones are irregular and blocky in outline, and most appear on canyon interfluves, canyon walls, and canyon floors in the lower reaches (Fig. 4). Cross-slope profiles of elevation change show that the deposition-dominated zones with irregular outlines can occur on the ridges of canyon interfluves (Fig. 6D). The irregular blocky zones dominated by deposition range in length from 0.2 to 2.0 km and in width from 0.2 to 1.0 km. The largest of these irregularly shaped zones is 1.5 km^2 (canyon C7).

5. Discussion

5.1 Reliability of detected elevation changes

Making repeat bathymetry measurements has been shown to be an effective means of analyzing different submarine sediment transport processes (e.g., Hughes Clarke et al., 1996; Hughes Clarke, 2016). However, it is important to test whether local site characteristics, particularly steep slope gradients, which make data acquisition difficult are in fact the cause of differences between datasets (Fox et al., 1992).

Prior to GPS ship navigation being common, the impact of slope gradients on differences between datasets was evaluated using a slope weighting factor (Chadwick et al., 1998, 2008, 2018). However, the wide application of precise GPS location has made the inclusion of such a weighting factor unnecessary. Nonetheless we have assessed the potential impact of slope and water depth on our measured elevation differences (Fig. 7). Our data show no obvious correlation between elevation change and slope gradient or elevation change and water depth. We therefore, conclude that neither slope nor water depth has had a significant impact on our detected elevation change and thus we have confidence in our results.

5.2 Interpretation of seismic facies

Previous studies have used integrated seismic and borehole analyses to understand the evolution of the canyons in the Pearl River Mouth Basin (Zhu et al., 2010; Sun et al., 2012; Gong et al., 2013; Yang et al., 2015, 2017; Zhou et al., 2015). Borehole data has verified that the chaotic high amplitude seismic reflectors and the transparent seismic facies which make up the canyon fill facies represent turbidites (Zhou et al., 2015) and debris flow deposits, respectively (Zhu et al., 2010; Gong et al., 2013). Meanwhile the high-amplitude reflectors which constrain these facies are thought to represent the incision surfaces of paleo-canyons (Zhu et al., 2010; Zhou et al., 2015).

In contrast to the channel fill facies, the contorted seismic facies which exist on the canyon walls (Fig. 3) exhibit a combination of characteristics which are indicative of

submarine landslides or slumps and therefore represent slope instabilities (Hampton et al., 1996). These facies show evidence of headscarps and glide surfaces which display as reflectors separating the displaced mass from the underlying strata (He et al., 2014). They also show evidence of normal faults indicative of material displacement and thus mass failures (He et al., 2014; Su et al., 2019).

Last, 3-D seismic and borehole studies have shown that the columnar/cone shaped transparent to chaotic seismic facies seen in Fig. 3. are representative of gas chimneys/fluid migration pathways which exist as a consequence of the abundance of gas hydrates which exist in the area (Sun et al., 2012; Yang et al., 2015, 2017).

5.3. Canyon ridge crescentic features

Numerous crescentic features have been identified on the ridges between the canyons (Fig. 2). Features with similar plan-view morphologies and scales have been observed in other settings (Migeon, et al., 2012; Zhong et al., 2015; Symons et al., 2016; Pope et al., 2018; among many others). Crescentic features such as those that are observed are thought to be predominantly generated by turbidity currents or slope instabilities. Where features are related to turbidity currents, the internal architecture of the bedforms is made up of regular ordered reflectors, which in the case of supercritical turbidity currents exhibit regular back-stepping beds which develop as the bedform migrates upstream (Migeon et al., 2001; Postma and Cartigny, 2014; Hage et al., 2018). They are also regularly found in bedform trains associated with fluctuating flow

properties (Cartigny et al., 2011). In contrast, where bedforms are related to slope instabilities a number of the following should be present; (1) a distinct headscarp; (2) a glide plane or surface; (3) listric normal faults; (4) offset or deformed internal reflectors, and; (5) a compressional/depositional zone (Bugge et al., 1988; Hampton et al., 1996; Masson et al., 2006; Chaytor et al., 2009). According to these criteria, previously published seismic and core data show that the majority of the scarps are likely related to slope instabilities (see He et al., 2014 and Su et al., 2019 for more details). Nonetheless, some features do indeed appear display upslope-migrating internal architecture but examples of this are limited (He et al., 2014). Moreover, the crescentic features do not exist in coherent trains with similar alignments but instead diverge either side of the canyon ridges further suggesting a slope instability origin (Fig. 2).

5.4 Sedimentary processes in the modern slope-confined canyons

The 2004/2018 and 2005/2018 repeat multibeam surveys reveal significant widespread and large volume erosion accompanied by local small volume deposition in the seven slope-confined submarine canyons in the study area. Ratios of erosion-dominated to deposition-dominated area within the canyons are 1 to 2.3 times greater (Tab. 2), and ratios of erosion volume to deposition volume range from 1.2 to 3.4 times greater. Average rates of erosion depth are also larger than average rates of deposition thickness. The dominance of erosional processes is typical for shelf-incised canyon systems, especially during sea level lowstands (Shepard, 1981; Posamentier and Walker,

2006; Covault and Graham, 2010). We will now discuss the mechanisms by which this erosion and deposition may have occurred in the slope-confined canyons during the present sea level highstand.

Sedimentary processes in submarine canyons are dominated by the activity of sediment gravity flows, especially turbidity currents (Shepard et al., 1966; Talling, 2014). These flows can be generated by three main mechanisms: plunging of sediment-laden river floodwaters, mass failure of unconsolidated or loosely consolidated sediments, or resuspension of sediment near the shelf edge by oceanographic processes (Piper and Normark, 2009; Talling et al., 2013; Talling, 2014). The different morphologies of the erosion-dominated and deposition-dominated zones of the submarine canyons in the study area imply different mechanisms of turbidity current generation.

5.4.1 Erosion in linear zones

The fact that the linear zones dominated by erosion occur mainly in the upper canyon reaches suggests that the turbidity currents responsible for these erosion marks may have originated on the shelf or upper slope, with their erosional power decreasing down-canyon. The plunging of hyperpycnal river water commonly triggers dilute and slow-moving flows (Talling, 2014), but the modern canyons in the study area are not presently connected to any river mouth. River-related flows therefore seem unlikely to have operated in the canyons during the 14-year study period.

Mass failure may occur on both gentle and steep submarine slopes (Talling, 2014).

In gently (< 2°) sloping areas (e.g., open continental slope and basin floor), such events are typically large (extending for several hundred kilometers and involving 100s-1000s km^3 of material) and infrequent (≥1 per a thousand years), triggering powerful canyon-flushing turbidity currents (Talling, 2014). In the case of the studied canyons, the occurrence of extensive erosion within a mere 14 years and the absence or unresolvable nature of linear erosion-dominated zones in the lower canyon reaches indicates that this form of infrequent mass failure is not likely the responsible agent. Submarine cables are also present further downslope of the canyons but are not known to have been broken by turbidity currents between 2004 and 2018 (Pope, personal communication, 2018) which also supports the absence of large powerful turbidity currents associated with large-scale slope failures or canyon flushing events (Piper et al., 1999; Allin et al., 2018). In steeper areas (e.g., delta lips), mass failures occur frequently (1 to 5 or more per year on modern delta-lips) (Talling et al., 2013; Talling, 2014; Clare et al., 2016; Hizzett et al., 2018). In the study area, bathymetric and seismic data indicate that a paleo-delta extends to the shelf edge (Lüdmann et al., 2001; Zhou et al., 2015; Wang et al., 2017). However, because the present Pearl River delta is confined to the river estuary (Wei and Wu, 2011), the paleo-delta is likely not receiving large volumes of river-derived sediment and mass failure on the paleo-delta lip is probably infrequent. This form of frequent mass failure is therefore also likely not responsible for the recent occurrence of turbidity currents and extensive upper-canyon erosion.

Sediment resuspension (e.g., by surface waves or internal waves) is another way

to generate powerful turbidity currents, in some places several times per year (Talling et al., 2013). In the northern continental shelf of the Dongsha Islands, the widespread occurrence of modern sand waves trending NE–SW (Wang, 2000) indicates energetic NW–SE ocean processes capable of moving coarse sand grains. The northern South China Sea is in fact the site of the world's largest and most powerful internal solitary waves (Ramp et al., 2004; Alford et al., 2015), with amplitudes of up to 240 m and northwestward propagation speeds of up to 2.9 m/s (Klymak et al., 2006; Huang et al., 2016). Internal solitary waves occur in the ocean's interior, due to difference in density between adjacent layers of water. In the northern South China Sea, internal solitary waves are generated diurnally by the interaction of tides and local bathymetry in the Luzon Strait (Fig. 8A, B) and propagate northwestward toward the Dongsha Islands and the coast of China (Alpers, 2014; Alford et al., 2015; Ma et al., 2016). These internal solitary waves occur at the water depth of up to 300–500 m (Hsu and Liu, 2000; Lien et al., 2014; Tang et al., 2015), and can significantly increase the flow velocity (e.g., more than 10 cm/s at ~2374 m; Dong et al., 2015) of the entire water column when they pass through (Huang et al., 2016).

During a 2011 field deployment in the nearby study area, observations of bottom currents (see locations in Fig. 8B) showed that internal solitary waves were the most powerful events to occur near seabed during the study period (Ma et al., 2016). These energetic waves propagated diurnally in the direction of approximately 290° (Fig. 8B), causing strong near-bottom (1 m above the seabed) currents (some exceeding 90 cm/s)

as the waves shoaled onto the shelf, west of the Dongsha Atoll (Fig. 8C; Ma et al., 2016). Such currents can suspend coarse sediments in the continental shelf and shelf edge areas (Ma et al., 2016). Many observations from around the globe have confirmed that internal solitary waves are capable of inducing bottom stresses sufficient to initiate sediment movement and resuspend seabed sediments, especially during wave shoaling and breaking (see review in Boegman and Stastna, 2019). In the study area, shoaling internal solitary waves that stir up waters dense with resuspended sediment are probably the dominant mechanism responsible for triggering turbidity currents that scour the upper canyon reaches.

Canyon Migration

The linear erosion-dominated zones occurring at the base of the eastern canyon walls are indicative of the continued eastward migration of these canyons (Figs. 4 and 6; Zhu et al., 2010; Zhou et al., 2015). These 14-year bathymetric indicators of migration are consistent with the longer-term canyon-fill migration seen in the seismic profiles (Fig. 3) and with observations from other seismic reflection studies in the area (Zhu et al., 2010; Gong et al., 2013; Zhou et al., 2015). This migration could be driven or influenced by processes such as bidirectional canyon migration, the effects of Coriolis forces, topographic steering of turbidity currents, and bottom currents. The first three possibilities can be readily ruled out. Submarine canyon evolution may include bidirectional (zig-zagging) migration (Posamentier and Walker, 2006), but no evidence of this behavior is found in the multibeam bathymetric or seismic reflection data of the

study area (Fig. 3; Zhu et al., 2010; Gong et al., 2013; Zhou et al., 2015). Coriolis forces can, in the Northern Hemisphere, cause mid- and high-latitude turbidity currents to veer to the right (Komar, 1969; Piper et al., 1983). In the case of the studied canyons, though, this effect would encourage westward, not eastward, migration. Topographic steering is also a weak candidate for driving the eastward migrations, as no large cross-cutting topographic features are evident in the study area (Figs. 3 and 4). The nearby Dongsha Islands (Figs. 1A and 8A) experienced two uplifts at the Miocene/Pliocene boundary and in the Pleistocene (Lüdmann and Wong, 1999), but this phenomenon too would tend to drive westward, not eastward, migration of the canyons.

Bottom currents may be a plausible cause of the observed canyon migration although without direct measurements of turbidity currents in these canyons uncertainty remains. The study area is affected by eastward regional water mass circulation (with current speeds <10 cm/s between 500 and 1500 m water depth; Tian et al., 2006; Yang et al., 2010). It is also affected by westward-propagating depression internal waves (waves with predominantly downward displacements) which originate at the Luzon Strait (Fig. 8A; Alford et al., 2015; Huang et al., 2016; Ma et al., 2016; Bai et al., 2017). These waves have been shown to generate reversing eastward near-bed currents with velocities of up to 40 cm/s at water depths of 481 m (mooring site in Fig. 8B) and 90 cm/s at water depths of 175 m (site B in Fig. 8B) (Ma et al., 2016; Boegman and Stastna, 2019). The variable strength of these currents will have a significant impact on their interaction with turbidity currents.

Flume tank (Eurotank in Utrecht University) experiments have shown that along-slope bottom current velocities larger than 15 cm/s are required to deflect unconfined depositional turbidity currents with velocities of between 1.0 to 1.4 m/s (Gong et al., 2018; The Drifters group, personal communication, 2019). Hence, the eastward regional water circulation would likely be too weak to steer confined and erosive turbidity currents which flow down the canyon if they have similar characteristics as those reported in other settings such as Mendocino (California) and Gaoping (Taiwan) canyons (Sumner and Paull, 2014; Hughes Clarke, 2016; Gavey et al., 2017; Paull et al., 2018; Vendettuoli et al., 2019). However, if turbidity current characteristics more closely resemble those reported in the Eel (northern California) or Fonera (in the Gulf of Lions) canyons (tens of cm/s), then even the low velocity regional water mass circulation may result in eastward deflection of turbidity currents (Puig et al., 2003; Palanques et al., 2006). In contrast, combined with the regional water circulation, the eastward near-bed current resulting from internal waves is likely to steer slow moving turbidity currents eastward along their down-canyon path and may even impact upon those flowing at higher velocities. This would likely result in preferential erosion along the eastern canyon walls which we observe and thus eastward canyon migration.

5.4.2 Erosion in block-shaped zones

The irregular, block-shaped zones dominated by erosion are widespread mainly in lower canyon reaches, indicating different modes of erosion in the upper and lower reaches. In the upper reaches, the blocky erosion-dominated zones occur sporadically

on the steep canyon walls, suggesting local mass failures (Fig. 3). Such events are common in submarine canyons worldwide (Masson et al., 2011; Biscara et al., 2013; Xu et al., 2013).

In the lower canyon reaches (water depths >～1000 m), the blocky erosion-dominated zones are widespread, both within and between the canyons (Fig. 4), suggesting that a regional mechanism for the development of these zone is responsible. The presence of gas hydrates, which are indicated by bottom-simulating reflectors (BSRs), and gas chimneys (Figs. 3C, D and 8B; Chen et al, 2016) suggesting gas/fluid migration are found at similar depths as confirmed by drilling in the study area (Yang et al., 2017). The correlation of gas hydrate presence and significant slope instabilities suggest a causal relationship may exist.

Gas hydrate processes, including accumulation, expansion, dissociation, and pipe structure formation have been proposed as triggers for slope instability events (Bugge et al., 1988; Sultan et al., 2004; Serié et al., 2012; Elger et al., 2018). Overpressure caused by fluid migration, especially in fine sediments, may trigger sediment deformation and mass failures (Bugge et al., 1988; Sultan et al., 2004; Serié et al., 2012; Elger et al., 2018). In the study area, the presence of gas chimneys and shallow gas (Fig. 3; Sun et al., 2012) indicate possible gas expansion and subsequent increases in overpressure (Bugge et al., 1988; Sultan et al., 2004). Gas hydrates in the study area also reduce the permeability of the sediments (Gao et al., 2012; Yang et al., 2017), thus potential leading to a build-up of overpressure below the gas hydrate stability zone

(Yang et al., 2015, 2017). Pipes in the study area (Sun et al., 2012) could transfer this overpressure to shallower sediments (Elger et al., 2018), which could in turn trigger sediment deformation and mass failures.

One possible implication is that the gas hydrate–bearing portion of the study area has a high risk of submarine geohazards, which must be taken into account in assessments of seabed stability. The erosion rate in the lower reaches is 3 to 13 times greater of that in the upper canyon reaches (Fig. 5D), perhaps indicating that slope instabilities have dominated the erosion in the slope-confined canyons in the study area.

5.4.3 Local deposition

The sporadically distributed local deposition around canyon walls in the upper reaches probably represents residual deposition of small-scale mass failures on steep canyon walls and from mass failures on the interfluves above (Figs. 2 and 3). Small-scale mass failure events are very common along the margins of ancient and modern submarine canyons, e.g., Var (Mas et al., 2010; Khripounoff et al., 2012), Nazare (Masson et al., 2011) canyons. In the lower reaches the identified deposition is likely linked predominantly to slope failures on the interfluves and supports the hypothesis that gas-hydrate related processes probably triggered sediment deformation (Fig. 4; Bugge et al., 1988; Sultan et al., 2004; Serié et al., 2012; Elger et al., 2018). However, linking the deposition with a specific process requires the acquisition of additional high resolution seismic data (He et al., 2014).

Deposition along the canyon floors appears minimal, although this may be a

consequence of the vertical resolution of our bathymetry data. Here, deposition is likely dominated by weak or waning turbidity currents (Komar, 1969) but the apparent lack of widespread accumulation apart from blockier deposits suggests that sediment has been transported further downslope or dispersed over a wider area.

5.5 Comparison with shelf-incised canyons

The modern average rates of erosion and deposition of the slope-confined canyons (0.7–0.8 m/yr and 0.5–0.8 m/yr in average, respectively) in the northern South China Sea are on the same order of magnitude as modern average rates estimated (also from repeat bathymetric surveys) for shelf-incised canyons on other continental margins (Fig. 5C). Cap Lopez Canyon, for example, on the Gabon continental margin of West Africa, experienced an average erosion rate of 1.2 m/yr and an average deposition rate of 0.5 m/yr over the 49 years between 1959 and 2008 (Biscara et al., 2013). Capbreton Canyon, in the Bay of Biscay, exhibited erosion rates of ~2 m/yr in average and deposition rates of ~1 m/yr in average over 15 years of observation, 1998–2003 (Mazières et al., 2014). Monterey Canyon, offshore California, has experienced erosion and deposition rates about 2 m/yr in average during a single year (2002–2003) (Smith et al., 2005). These examples illustrate that rates of sedimentary processes in shelf-incised canyons may be matched in some slope-confined canyons, even during the present sea level highstand.

The triggering mechanisms for erosion in the two environments are, however, different. On present-day shelf-incised canyons, river-fed sedimentation, ocean waves,

and tides are able to generate frequent turbidity currents (e.g., Mazières et al., 2014; Talling, 2014; Gavey et al., 2017; Smith et al., 2018). In this study of slope-confined canyons, for the first time, we identify the shoaling of internal solitary waves as possibly the major trigger for turbidity currents in the upper reaches. In the lower reaches, activity of gas hydrates may have contributed to the generation of slope instabilities, which cause much larger volume of erosion than turbidity currents. These findings suggest that local, site-specific oceanographic and geological processes and features can significantly increase sedimentary activity within and near submarine canyons.

6. Conclusions

Bathymetric surveys of seven slope-confined canyons in the Pearl River Mouth Basin, South China Sea, conducted in 2004, 2005 and 2018, show that erosion strongly dominated local sedimentary processes during the intervening 14 years. The least erosional canyon (by area) experienced erosion over nearly 44% of its total area, while the most erosional canyon experienced erosion over nearly 56% of its total area. Average rate of erosion in volume ranged from 31×10^6 m^3/yr to 52×10^6 m^3/yr. Average rate of erosion in thickness ranged from about 0.7 m/yr to 0.8 m/yr. Deposition-dominated zones, which were scattered along the canyon walls and floors, occupied 22–45% of any canyon's area. Erosion-dominated to deposition-dominated areas were 1 to 2.3 times greater in individual canyons, and ratios of erosion to deposition rate in

volume ranged from 1.2 to 3.4. Average rate of vertical deposition ranged from about 0.5 to 0.8 m/yr.

In upper canyon reaches, erosion tended to leave linear scars along the canyon axes; at greater depths, blocky chunks of sediment had been widely removed from the steep canyon walls and interfluves. The frequent shoaling of energetic internal solitary waves onto the shelf is probably responsible for upper canyon scouring by triggering turbidity currents. The westward propagating powerful internal solitary waves of depression likely induce eastward canyon migration by generating rapid near-bed eastward currents enhanced by slow eastward regional water circulation. Overpressure associated with activity of abundant gas hydrates (accumulation, expansion, dissolution, gas chimneys and pipes) are likely responsible for triggering slope instabilities and widespread erosion in lower canyon reaches. The rate of erosion in the lower canyon likely dominated by slope instabilities was 3 to 13 times greater than the upper canyons where turbidity currents were the predominant mechanism of sediment transport.

High rates of sedimentary processes currently may occur in some slope-confined submarine canyons, even during sea level highstands. These findings suggest that local, site-specific oceanographic and geological features can significantly influence the level of sedimentary activity in submarine canyon systems.

7. Acknowledgements

We are grateful to Second Institute of Oceanography, Ministry of Natural Resources,

China, and Guangzhou Marine Geological Survey for permission to use these data and publish this work. This research was funded by the National Program on Global Change and Air-Sea Interaction, SOA (grants GASI-GEOGE-05 and GASI-GEOGE-01) and the National Natural Science Foundation of China (grants 41706043 and 41830540). We also thank Dr. Xiaochuan Ma for providing us the figure of the near-bed current observation around the study area. The first author thanks Prof. Charles K. Paull for his constructive suggestions regarding the initial version of this paper, and thanks Prof. William W. Chardwick for his constructive suggestions on the effect of slope on elevation change. We thank the editor Yongqiang Zong, Michael Clare and an anonymous reviewer for their in depth reviews and comments which greatly improved this manuscript.

References

Alford, M.H., Peacock, T., MacKinnon, J.A., Nash, J.D., Buijsman, M.C., Centuroni, L.R., Chao, S.-Y., Chang, M.-H., Farmer, D.M., Fringer, O.B., Fu, K.-H., Gallacher, P.C., Graber, H.C., Helfrich, K.R., Jachec, S.M., Jackson, C.R., Klymak, J.M., Ko, D.S., Jan, S., Johnston, T.M.S., Legg, S., Lee, I.H., Lien, R.-C., Mercier, M.J., Moum, J.N., Musgrave, R., Park, J.-H., Pickering, A.I., Pinkel, R., Rainville, L., Ramp, S.R., Rudnick, D.L., Sarkar, S., Scotti, A., Simmons, H.L., St Laurent, L.C., Venayagamoorthy, S.K., Wang, Y.-H., Wang, J., Yang, Y.J., Paluszkiewicz, T., Tang, T.-Y., 2015. The formation and fate of

internal waves in the South China Sea. Nature, 521(7550), 65–69.

Allin, J.R., Hunt, J.E., Clare, M.A. and Talling, P.J., 2018. Eustatic sea-level controls on the flushing of a shelf-incising submarine canyon. Geol. Soc. Am. Bull. 130(1-2), 222–237.

Alpers, W., 2014. Ocean Internal Waves. In: E.G. Njoku (Ed.), Encyclopedia of Remote Sensing. Springer New York, New York, NY, pp. 433–437.

Azpiroz-Zabala, M., Cartigny, M.J.B., Talling, P.J., Parsons, D.R., Sumner, E.J., Clare, M.A., Simmons, S.M., Cooper, C.K., Pope, E.L., 2017. Newly recognized turbidity current structure can explain prolonged flushing of submarine canyons. Sci. Adv. 3(10).

Bai, Y., Song, H., Guan, Y., Yang, S., 2017. Estimating depth of polarity conversion of shoaling internal solitary waves in the northeastern South China Sea. Cont. Shelf Res. 143, 9–17.

Biscara, L., Mulder, T., Hanquiez, V., Marieu, V., Crespin, J., Braccini, E., Garlan, T., 2013. Morphological evolution of Cap Lopez Canyon (Gabon): Illustration of lateral migration processes of a submarine canyon. Mar. Geol. 340, 49–56.

Boegman, L., Stastna, M., 2019. Sediment Resuspension and Transport by Internal Solitary Waves. Annu. Rev. Fluid Mech. 51, 129–154.

Bugge, T., Belderson, R., Kenyon, N., 1988. The storegga slide. Phil. Trans. R. Soc. Lond. A, 325(1586), 357–388.

Burgess, P.M., Hovius, N., 1998. Rates of delta progradation during highstands: consequences for timing of deposition in deep-marine systems. J. Geol. Soc. 155(2), 217–222.

Calder, B.R., Mayer, L.A. 2003. Automatic processing of high-rate, high-density multibeam echosounder data. Geochem. Geophs. Geosyst. 4(6).

Cartigny, M.J.B., Postma, G., van den Berg, J.H., Mastbergen, D.R. 2011. A comparative study of sediment waves and cyclic steps based on geometries, internal structures and numerical modeling. Mar. Geol. 280 (1-4), 40–56.

Chadwick Jr, W. W., Embley, R. W., Shank, T. M., 1998. The 1996 Gorda Ridge eruption: Geologic mapping, sidescan sonar, and SeaBeam comparison results. Deep Sea Res. Part II Top. Stud. Oceanogr. 45(12), 2547–2569.

Chadwick, W.W., Wright, I.C., Schwarz‐Schampera, U., Hyvernaud, O., Reymond, D. and De Ronde, C.E.J., 2008. Cyclic eruptions and sector collapses at Monowai submarine volcano, Kermadec arc: 1998–2007. Geochem. Geophys. Geosyst. 9(10).

Chadwick Jr, W. W., Merle, S. G., Baker, E. T., et al., 2018. A recent volcanic eruption discovered on the central Mariana back-arc spreading center. Frontiers in Earth Science, 6, 172.

Chaytor, J.D., Uri, S., Solow, A.R. and Andrews, B.D., 2009. Size distribution of submarine landslides along the US Atlantic margin. Mar. Geol. 264(1-2), 16–27.

Chen, D., Wang, X., Völker, D., Wu, S., Wang, L., Li, W., Li, Q., Zhu, Z., Li, C., Qin, Z., Sun, Q., 2016. Three dimensional seismic studies of deep-water hazard-related features on the northern slope of South China Sea. Mar. Pet. Geol. 77, 1125–1139.

Clare, M., Clarke, J.H., Talling, P., Cartigny, M., Pratomo, D., 2016. Preconditioning and triggering of offshore slope failures and turbidity currents revealed by most

detailed monitoring yet at a fjord-head delta. Earth Planet. Sci. Lett. 450, 208–220.

Covault, J.A., Graham, S.A., 2010. Submarine fans at all sea-level stands: Tectono-morphologic and climatic controls on terrigenous sediment delivery to the deep sea. Geology, 38(10), 939–942.

Deptuck, M.E., Steffens, G.S., Barton, M., Pirmez, C., 2003. Architecture and evolution of upper fan channel-belts on the Niger Delta slope and in the Arabian Sea. Mar. Pet. Geol. 20(6), 649–676.

Dong, J., Zhao, W., Chen, H., Meng, Z., Shi, X., Tian, J., 2015. Asymmetry of internal waves and its effects on the ecological environment observed in the northern South China Sea. Deep Sea Res. Part I Oceanogr. Res. Pap. 98, 94–101.

Elger, J., Berndt, C., Rüpke, L., Krastel, S., Gross, F., Geissler, W.H., 2018. Submarine slope failures due to pipe structure formation. Nat. Commun. 9(1).

Fox, C.G., Chadwick, W.W., Embley, R.W., 1992. Detection of changes in ridge-crest morphology using repeated multibeam sonar surveys. J. Geophys. Res. Solid Earth. 97(B7), 11149–11162.

Fyfe, J.A., Selby, I.C., Plater, A.J., Wright, M.R. 1999. Erosion and sedimentation associated with the last sea level rise offshore Hong Kong, South China Sea. Quat. Int. 55 (1), 93–100.

Gao, H., Zhong, G., Liang, J., Guo, Y., 2012. Estimation of gas hydrate saturation with modified Biot-Gassmann theory: a case from northern South China Sea. Mar. Geol. Quat. Geol. 32, 83–88 (in Chinese).

Gavey, R., Carter, L., Liu, J.T., Talling, P.J., Hsu, R.T., Pope, E.L., Evans, G., 2017. Frequent sediment density flows during 2006 to 2015, triggered by competing seismic and weather events: Observations from subsea cable breaks off southern Taiwan. Mar. Geol. 384, 147–158.

Gong, C., Wang, Y., Rebesco, M., Salon, S. and Steel, R.J., 2018. How do turbidity flows interact with contour currents in unidirectionally migrating deep-water channels?. Geology, 46(6), pp.551-554.

Gong, C., Wang, Y., Zhu, W., Li, W., Xu, Q., 2013. Upper Miocene to Quaternary unidirectionally migrating deep-water channels in the Pearl River Mouth Basin, northern South China Sea. Am. Assoc. Pet. Geol. Bull. 97(2), 285–308.

Gu, Q., Rao, K., Li, X., Xu, X., Wang, J., Zhu, Q., 1990. Remote Sensing Application in Lingdingyang Estuary. Chinese Science Press, Beijing (in Chinese).

Hage, S., Cartigny, M.J.B, Clare, M.A., Sumner, E.J., Vendettuoli, D., Hughes Clarke, J.E., Hubbard, S.M., Talling, P.J., Lintern, D.G., Stacey, C.D., Englert, R.G., 2018. How to recognise crescentic bedforms formed by supercritical turbidity currents in the geologic record: Insights from active submarine channels. Geology, 46 (6), 563–566.

Hampton, M.A., Lee, H.J. and Locat, J., 1996. Submarine landslides. Rev. Geophys. 34(1), 33–59.

Hare, R., Godin, A., Mayer, L.A. 1995. Accuracy estimation of Canadian swath (Multi-beam) and sweep (Multi-Transducer) sounding systems. Technical Report, Canadian Hydrography Service, Ottawa, Ontario.

Harris, P.T., Whiteway, T., 2011. Global distribution of large submarine canyons: Geomorphic differences between active and passive continental margins. Mar. Geol. 285(1-4), 69–86.

He, Y., Zhong, G., Wang, L., Kuang, Z., 2014. Characteristics and occurrence of submarine canyon-associated landslides in the middle of the northern continental slope, South China Sea. Mar. Pet. Geol. 57, 546–560.

Hizzett, J.L., Clarke, J.E.H., Sumner, E.J., Cartigny, M.J.B., Talling, P.J., Clare, M.A., 2018. Which triggers produce the most erosive, frequent and longest runout turbidity currents on deltas ? Geophys. Res. Lett. 45(2), 855–863.

Hsu, M.-K., Liu, A.K., 2000. Nonlinear internal waves in the South China Sea. Can. J. Rem. Sens. 26(2), 72–81.

Huang, X., Chen, Z., Zhao, W., Zhang, Z., Zhou, C., Yang, Q., Tian, J., 2016. An extreme internal solitary wave event observed in the northern South China Sea. Sci. Rep. 6.

Huang, J., Song, C., 1981. A richly endowed coastal zone. Ren. Hua. 11, 1–5 (in Chinese).

Hughes Clarke, J. E., Mayer, L. A., Wells, D. E., 1996. Shallow-water imaging multibeam sonars: a new tool for investigating seafloor processes in the coastal zone and on the continental shelf. Mar. Geophys. Res. 18(6), 607–629.

Hughes Clarke, J. E., 2016. First wide-angle view of channelized turbidity currents links migrating cyclic steps to flow characteristics. Nat. Commun. 7, 11896.

Khripounoff, A., Vangriesheim, A., Crassous, P., Etoubleau, J., 2009. High frequency of sediment gravity flow events in the Var submarine canyon (Mediterranean Sea). Mar. Geol. 263, 1–6.

Khripounoff, A., Crassous, P., Bue, N.L., Dennielou, B., Jacinto, R.S., 2012. Different types of sediment gravity flows detected in the Var submarine canyon (northwestern Mediterranean Sea). Prog. Oceanogr. 106, 138–153.

Klymak, J.M., Pinkel, R., Liu, C.T., Liu, A.K., David, L., 2006. Prototypical solitons in the South China Sea. Geophys. Res. Lett. 35(11).

Komar, P.D., 1969. The channelized flow of turbidity currents with application to Monterey Deep‐Sea Fan Channel. J.Geophys. Res. 74(18), 4544–4558.

Le Friant, A., Deplus, C., Boudon, G., Feuillet, N., Trofimovs, J., Komorowski, J. C., ... & Ryan, G. (2010). Eruption of Soufrière Hills (1995–2009) from an offshore perspective: Insights from repeated swath bathymetry surveys. Geophys. Res.

Lett. 37(19).

Li, C.F., Xu, X., Lin, J., Sun, Z., Zhu, J., Yao, Y., Zhao, X., Liu, Q., Kulhanek, D.K., Wang, J., 2014. Ages and magnetic structures of the South China Sea constrained by deep tow magnetic surveys and IODP Expedition 349. Geochem. Geophys. Geosyst. 15(12), 4958–4983.

Lien, R.-C., Henyey, F., Ma, B., Yang, Y.J., 2014. Large-amplitude internal solitary waves observed in the northern South China Sea: properties and energetics. J. Phys. Oceanogr. 44(4), 1095–1115.

Lüdmann, T., Wong, H. K., 1999. Neotectonic regime on the passive continental margin of the northern South China Sea. Tectonophysics, 311(1-4), 113–138.

Lüdmann, T., Kin Wong, H., Wang, P., 2001. Plio–Quaternary sedimentation processes and neotectonics of the northern continental margin of the South China Sea. Mar. Geol. 172(3–4), 331–358.

Lurton, X. 2003. Theoretical modelling of acoustic measurement accuracy for swath bathymetric sonars. Int. Hydrogr. Rev. 4 (2), 17–30.

Lurton, X., Augustin, J.M. 2010. A measurement quality factor for swath bathymetry sounders. IEEE J. Ocean. Eng. 35 (4), 852–862.

Ma, X., Yan, J., Hou, Y., Lin, F., Zheng, X., 2016. Footprints of obliquely incident internal solitary waves and internal tides near the shelf break in the northern South China Sea. J. Geophys. Res. Oceans. 121(12), 8706–8719.

Mas, V., Mulder, T., Dennielou, B., Schmidt, S., Khripounoff, A., Savoye, B., 2010. Multiscale spatio-temporal variability of sedimentary deposits in the Var turbidite system (North-Western Mediterranean Sea). Mar. Geol. 275, 37–52.

Masson, D.G., Harbitz, C.B., Wynn, R.B., Pedersen, G. and Løvholt, F., 2006. Submarine landslides: processes, triggers and hazard prediction. Philos. Trans. A. Math. Phys. Eng. Sci. 364(1845), 2009–2039.

Masson, D., Huvenne, V., de Stigter, H., Arzola, R., LeBas, T., 2011. Sedimentary processes in the middle Nazaré Canyon. Deep Sea Res. Part II Top. Stud. Oceanogr. 58(23-24), 2369–2387.

Mazières, A., Gillet, H., Castelle, B., Mulder, T., Guyot, C., Garlan, T., Mallet, C., 2014. High-resolution morphobathymetric analysis and evolution of Capbreton

submarine canyon head (Southeast Bay of Biscay—French Atlantic Coast) over the last decade using descriptive and numerical modeling. Mar. Geol. 351, 1–12.

Migeon, S., Cattaneo, A., Hassoun, V., Dano, A., Casedevant, A. and Ruellan, E., 2012. Failure processes and gravity-flow transformation revealed by high-resolution AUV swath bathymetry on the Nice continental slope (Ligurian Sea), In: Yasuhiro et al. (Eds.), Submarine Mass Movements and Their Consequences. Springer, Dordrecht, pp. 451–461.

Migeon, S., Savoye, B., Zanella, E., Mulder, T., Faugères, J.C. and Weber, O., 2001. Detailed seismic-reflection and sedimentary study of turbidite sediment waves on the Var Sedimentary Ridge (SE France): significance for sediment transport and deposition and for the mechanisms of sediment-wave construction. Mar. Pet. Geol. 18(2), 179–208.

Mountjoy, J.J., Howarth, J.D., Orpin, A.R., Barnes, P.M., Bowden, D.A., Rowden, A.A., Schimel, A.C., Holden, C., Horgan, H.J., Nodder, S.D. and Patton, J.R., 2018. Earthquakes drive large-scale submarine canyon development and sediment supply to deep-ocean basins. Sci. adv. 4(3), 3748.

Mulder, T., Zaragosi, S., Garlan, T., Mavel, J., Cremer, M., Sottolichio, A., Sénéchal, N., Schmidt, S., 2012. Present deep-submarine canyons activity in the Bay of Biscay (NE Atlantic). Mar. Geol. 295, 113–127.

Normark, W.R., Carlson, P.R., 2003. Giant submarine canyons: Is size any clue to their importance in the rock record? In: Chan, M.A., and Archer, A.W. (Eds.), Extreme depositional environments: Mega end members in geologic time. Boulder, Colorado, pp. 175–190.

Palanques, A., Martín, J., Puig, P., Guillén, J., Company, J.B. and Sardà, F., 2006. Evidence of sediment gravity flows induced by trawling in the Palamós (Fonera) submarine canyon (northwestern Mediterranean). Deep Sea Res. Part I Oceanogr. Res. Pap. 53(2), 201–214.

Paull, C., Ussler III, W., Greene, H., Keaten, R., Mitts, P., Barry, J., 2003. Caught in the act: the 20 December 2001 gravity flow event in Monterey Canyon. Geo-Mar. Lett., 22, 227–232.

Paull, C.K., Talling, P.J., Maier, K.L., Parsons, D., Xu, J., Caress, D.W., Gwiazda, R., Lundsten, E.M., Anderson, K., Barry, J.P. and Chaffey, M., 2018. Powerful turbidity currents driven by dense basal layers. Nat. commun. 9(1), 4114.

Piper, D.J., Stow, D.A., Normark, W.R., 1983. The Laurentian fan: Sohm abyssal plain. Geo-Mar. Lett. 3(2-4), 141–146.

Piper, D.J., Cochonat, P. and Morrison, M.L., 1999. The sequence of events around the epicentre of the 1929 Grand Banks earthquake: initiation of debris flows and turbidity current inferred from sidescan sonar. Sedimentology, 46(1), 79–97.

Piper, D.J.W., Normark, W.R., 2009. Processes that initiate turbidity currents and their influence on turbidites: A marine geology perspective. J. Sediment. Res. 79(6), 347–362.

Pope, E.L., Jutzeler, M., Cartigny, M.J.B., Shreeve, J., Talling, P.J., Wright, I.C., Wysoczanski, R.J. 2018. Origin of spectacualr fields of submarine sediment waves around volcanic islands. Earth Planet. Sci. Lett. 493, 12–24.

Posamentier, H.W., Kolla, V., 2003. Seismic geomorphology and stratigraphy of depositional elements in deep-water settings. J. Sediment. Res. 73(3), 367–388.

Posamentier, H.W., Walker, R.G., 2006. Facies models revisited. SEPM, Tulsa.

Postma, G. and Cartigny, M.J., 2014. Supercritical and subcritical turbidity currents and their deposits—A synthesis. Geology, 42(11), 987–990.

Puig, P., Ogston, A.S., Mullenbach, B.L., Nittrouer, C.A. and Sternberg, R.W., 2003. Shelf-to-canyon sediment-transport processes on the Eel continental margin (northern California). Mar. Geol. 193(1-2), 129–149.

Pratson, L.F., Ryan, W.B.F., Mountain, G.S., Twichell, D.C., 1994. Submarine canyon initiation by downslope-eroding sediment flows: Evidence in late Cenozoic strata on the New Jersey continental slope. Geol. Soc. Am. Bull. 106(3), 395–412.

Qiao, S., Su, M., Kuang, Z., Yang, R., Liang, J., Wu, N., 2015. Canyon-related undulation structures in the Shenhu area, northern South China Sea. Mar. Geophys. Res. 36, 243–252.

Ramp, S. R., Tang, T. Y., Duda, T. F., Lynch, J. F., Liu, A. K., Chiu, C., Bahr, F.L., Kim, H., Yang, Y., 2004. Internal solitons in the northeastern south China Sea. Part I: sources and deep water propagation. IEEE J. Ocean. Eng. 29(4), 1157–1181.

Reading, H., Richards, M., 1994. The classification of deep-water siliciclastic

depositional systems by grain size and feeder systems. Am. Assoc. Pet. Geol. Bull. 78(5), 792–822.

Schimel, A.C., Lerodiaconou, D., Hulands, L., Kennedy, D.M. 2015. Accounting for uncertainty in volumes of seabed change measured with repeat multibeam sonar surveys. Con. Shelf Res. 111, 52–68.

Serié, C., Huuse, M. and Schødt, N.H., 2012. Gas hydrate pingoes: Deep seafloor evidence of focused fluid flow on continental margins. Geology, 40(3), 207–210.

Shepard, F.P., 1981. Submarine canyons: multiple causes and long-time persistence. Am. Assoc. Pet. Geol. Bull. 65(6), 1062–1077.

Shepard, F.P., Dill, R.F., 1966. Submarine canyons and other sea valleys. J. Geol. 77(6).

Smith, D.P., Ruiz, G., Kvitek, R., Iampietro, P.J., 2005. Semiannual patterns of erosion and deposition in upper Monterey Canyon from serial multibeam bathymetry. Geol. Soc. Am. Bull. 117(9–10), 1123–1133.

Smith, M.E., Werner, S.H., Buscombe, D., Finnegan, N.J., Sumner, E.J., Mueller, E.R., 2018. Seeking the shore: Evidence for active submarine canyon head incision

due to coarse sediment supply and focusing of wave energy. Geophys. Res. Lett. 45(22), 12–403.

Su, M., Alves, T. M., Li, W., et al., 2019. Reassessing two contrasting Late Miocene-Holocene stratigraphic frameworks for the Pearl River Mouth Basin, northern South China Sea. Mar. Pet. Geol. 102, 899–913.

Sultan, N., Cochonat, P., Foucher, J.-P., Mienert, J., 2004. Effect of gas hydrates melting on seafloor slope instability. Mar. Geol. 213(1–4), 379–401.

Sumner, E.J., Paull, C.K., 2014. Swept away by a turbidity current in Mendocino submarine canyon, California. Geophys. Res. Lett. 41(21), 7611–7618.

Sun, Q., Wu, S., Cartwright, J., Dong, D., 2012. Shallow gas and focused fluid flow systems in the Pearl River Mouth Basin, northern South China Sea. Mar. Geol. 315, 1–14.

Symons, W.O., Sumner, E.J., Talling, P.J., Cartigny, M.J., Clare, M.A. 2016. Large-scale sediment waves and scours on the modern seafloor and their implications for the prevalence of supercritical flows. Mar. Geol. 371, 130–148.

Talling, P.J., 2014. On the triggers, resulting flow types and frequencies of subaqueous sediment density flows in different settings. Mar. Geol. 352(0), 155–182.

Talling, P.J., Paull, C.K., Piper, D.J.W., 2013. How are subaqueous sediment density flows triggered, what is their internal structure and how does it evolve? Direct observations from monitoring of active flows. Earth Sci. Rev. 125(0), 244–287.

Tang, Q., Hobbs, R., Wang, D., Sun, L., Zheng, C., Li, J., Dong, C., 2015. Marine seismic observation of internal solitary wave packets in the northeast South China Sea. J. Geophys. Res. Ocean. 120(12), 8487–8503.

Taylor, B., Hayes, D.E., 1980. The tectonic evolution of the South China Basin. Geophys. Monogr. Ser. 23, 89–104.

Tian, J., Yang, Q., Liang, X., Xie, L., Hu, D., Wang, F., Qu, T., 2006. Observation of Luzon Strait transport. Geophys. Res. Lett. 33(19).

Vail, P., Mitchum Jr, R., Thompson III, S., 1977. Seismic stratigraphy and global changes of sea level: Part 3. Relative changes of sea level from Coastal Onlap. In: Payton, C.E. (Eds.), Seismic Stratigraphy-Applications to Hydrocarbon exploration. The American Association of Petroleum Geologists, Tulsa, pp.

63–72.

Vendettuoli, D., Clare, M.A., Clarke, J.H., Vellinga, A., Hizzet, J., Hage, S., Cartigny, M.J.B., Talling, P.J., Waltham, D., Hubbard, S.M. and Stacey, C., 2019. Daily bathymetric surveys document how stratigraphy is built and its extreme incompleteness in submarine channels. Earth Planet. Sci. Lett. 515, 231-247.

Wang, J., Huang, W., Yang, J., Zhang, H., 2011. The internal waves' distribution of whole South China Sea extracted from ENVISAT and ERS-2 SAR images. In: Bostater, C., Bostater Jr, C. R., Mertikas, S. P., Neyt, X., Nichol, C., Aldred, O. (Eds.), Remote Sensing of the Ocean, Sea Ice, Coastal Waters, and Large Water Regions 2011. SPIE, Washington, pp. 81751G.

Wang, P., Li, Q., 2009. The South China Sea: Paleoceanography and Sedimentology. Springer, Demand.

Wang, W.J., 2000. Propagation of tidal waves and development of sea-bottom sand ridges and sand ripples in northern South China Sea. Trop. Oceanol. 19 (1), 1–7 (in Chinese).

Wang, X., Wang, Y., He, M., Chen, W., Zhuo, H., Gao, S., Wang, M., Zhou, J., 2017.

Genesis and evolution of the mass transport deposits in the middle segment of the Pearl River canyon, South China Sea: Insights from 3D seismic data. Mar. Pet. Geol. 88, 555–574.

Wei, X., Wu, C., 2011. Holocene delta evolution and sequence stratigraphy of the Pearl River Delta in South China. Sci. China Earth Sci. 54(10), 1523.

Wright, I. C., Chadwick Jr, W. W., de Ronde, C. E., Reymond, D., Hyvernaud, O., Gennerich, H. H., ... & Bannister, S. C. (2008). Collapse and reconstruction of Monowai submarine volcano, Kermadec arc, 1998–2004. J. Geophys. Res. Solid Earth, 113(B8).

Wynn, R.B., Cronin, B.T., Peakall, J., 2007. Sinuous deep-water channels: Genesis, geometry and architecture. Mar. Pet. Geol. 24(6–9), 341–387.

Wu, Z., Milliman, J. D., Zhao, D., Zhou, J., Yao, C., 2014. Recent geomorphic change in LingDing Bay, China, in response to economic and urban growth on the Pearl River Delta, Southern China. Glob. Planet. Change, 123, 1–12.

Wu, Z., Milliman, J. D., Zhao, D., Cao, Z., Zhou, J., Zhou, C., 2018. Geomorphologic changes in the lower Pearl River Delta, 1850–2015, largely due to human

activity. Geomorphology, 314, 42–54.

Xu, J., Barry, J.P., Paull, C.K., 2013. Small-scale turbidity currents in a big submarine canyon. Geology, 41(2), 143–146.

Xu, J., Noble, M., Rosenfeld, L., 2004. In-situ measurements of velocity structure within turbidity currents. Geophys. Res. Lett. 31(9), L09311.

Yang, Q., Tian, J., Zhao, W., 2010. Observation of Luzon Strait transport in summer 2007. Deep Sea Res. Part I Oceanogr. Res. Pap. 57(5), 670–676.

Yang, S., Lei, Y., Liang, J., Holland, M., Schultheiss, P., Lu, J., Wei, J., 2017. Concentrated Gas Hydrate in the Shenhu Area, South China Sea: Results From Drilling Expeditions GMGS3 & GMGS4. Proceedings of 9th International Conference on Gas Hydrates. Denver, Paper No. 105.

Yang, S., Zhang, M., Liang, J., Lu, J., Zhang, Z., Holland, M., Schultheiss, P., Fu, S., Sha, Z., 2015. Preliminary results of China's third gas hydrate drilling expedition: A critical step from discovery to development in the South China Sea. Cent. Nat. Gas Oil. 412, 386–7614.

Zhang, Y., Liu, Z., Zhao, Y., Colin, C., Zhang, X., Wang, M., Zhao, S., Kneller, B., 2018. Long-term in situ observations on typhoon-triggered turbidity currents in the deep sea. Geology, 46(8), 675–678.

Zhao, D., Wu, Z., Zhou, J., Li, J., Shang, J., Li, S., 2015. A new method of automatic SVP optimization based on MOV algorithm. Mar. Geod. 38(3), 225–240.

Zhao D, Wu Z, Li J, et al., 2019. The Key Technology and Application of Parameter Optimization Combined CUBE and Surface Filter. Acta Geod. Cartogr. Sin. 2019, 48(2), 245–255 (In Chinese).

Zhou, W., Wang, Y., Gao, X., Zhu, W., Xu, Q., Xu, S., Cao, J., Wu, J., 2015. Architecture, evolution history and controlling factors of the Baiyun submarine canyon system from the middle Miocene to Quaternary in the Pearl River Mouth Basin, northern South China Sea. Mar. Pet. Geol. 67, 389–407.

Zhong, G., Cartigny, M.J.B, Kuang, Z., Wang, L. 2015. Cyclic steps along the South Taiwan Shoal and West Penghu submarine canyons on the northeastern continental slope of the South China Sea. Geo. Soc. Am. Bull. 127, 804–824.

Zhu, M., Graham, S., Pang, X., McHargue, T., 2010. Characteristics of migrating submarine canyons from the middle Miocene to present: Implications for

paleoceanographic circulation, northern South China Sea. Mar. Pet. Geol. 27(1), 307–319.

Tables

Table 1

General morphologic parameters of seven submarine canyons in the study area

Canyon name	Water depth at canyon head (m)	Water depth at canyon mouth (m)	Length (km)	Width (km)	Axis slope, from upper to lower canyon (degree)	Canyon area (km^2)
C6	580	--*	>12	1.5 - 1.6	4.5 – 8.6 – 1.0	22.1**
C7	538	1573	37	1.2 - 4.8	4.5 – 1.0	131.7
C8	866	1631	24	1.1 - 2.8	2.9 – 0.8	63.4
C9	574	1405	36	1.4 - 4.3	3.0 – 4.5 – 1.6	99.8
C10	610	1638	40	1.7 - 4.7	2.9 – 5.7 – 1.0	128.2
C11	865	1425	23	2.3 - 3.4	3.7 – 5.6 – 0.9	93.4
C12	689	1663	38	1.5 - 3.1	4.9 – 0.8	111.4

*Mouth of canyon C6 was not included in the bathymetric surveys

**Lower reach of canyon C6 was not included in the bathymetric surveys

Table 2

Characteristics of identified erosion and deposition

Canyon name	Average erosion thickness (m)		Erosion-dominated area (km^2)		Eroded volume ($\times 10^6$ m^3)		Average deposition thickness (m)		Deposition-dominated area (km^2)		Deposited volume ($\times 10^6$ m^3)	
	2004-2018	***2005-2018***	***2004-2018***	***2005-2018***	***2004-2018***	***2005-2018***	***2004-2018***	***2005-2018***	***2004-2018***	***2005-2018***	***2004-2018***	***2005-2018***
C6	10.7	--*	9.9	--*	106.6	--*	8.2	--*	10.0	--*	82.0	--*
C7	7.0	12.2	26.0	40.8	182.8	496.3	6.9	14.1	21.5	16.0	148.3	226.2
C8	8.2	12.3	3.9	31.2	32.1	384.4	9.2	8.1	8.2	8.9	72.5	72.7
C9	6.9	11.1	16.6	26.8	114.8	297.2	8.7	10.4	23.2	14.6	202.8	151.7
C10	9.4	9.9	19.4	50.9	183.1	505.7	9.8	11.2	15.8	17.2	155.5	193.5
C11	9.5	10.9	8.5	42.1	80.7	460.7	9.4	10.9	11.0	14.0	102.6	142.2
C12	8.9	9.5	16.3	41.6	145.7	395.2	7.1	6.2	13.5	11.4	95.8	70.0

*Lower reach of canyon C6 was not included in the bathymetric surveys

Figure captions

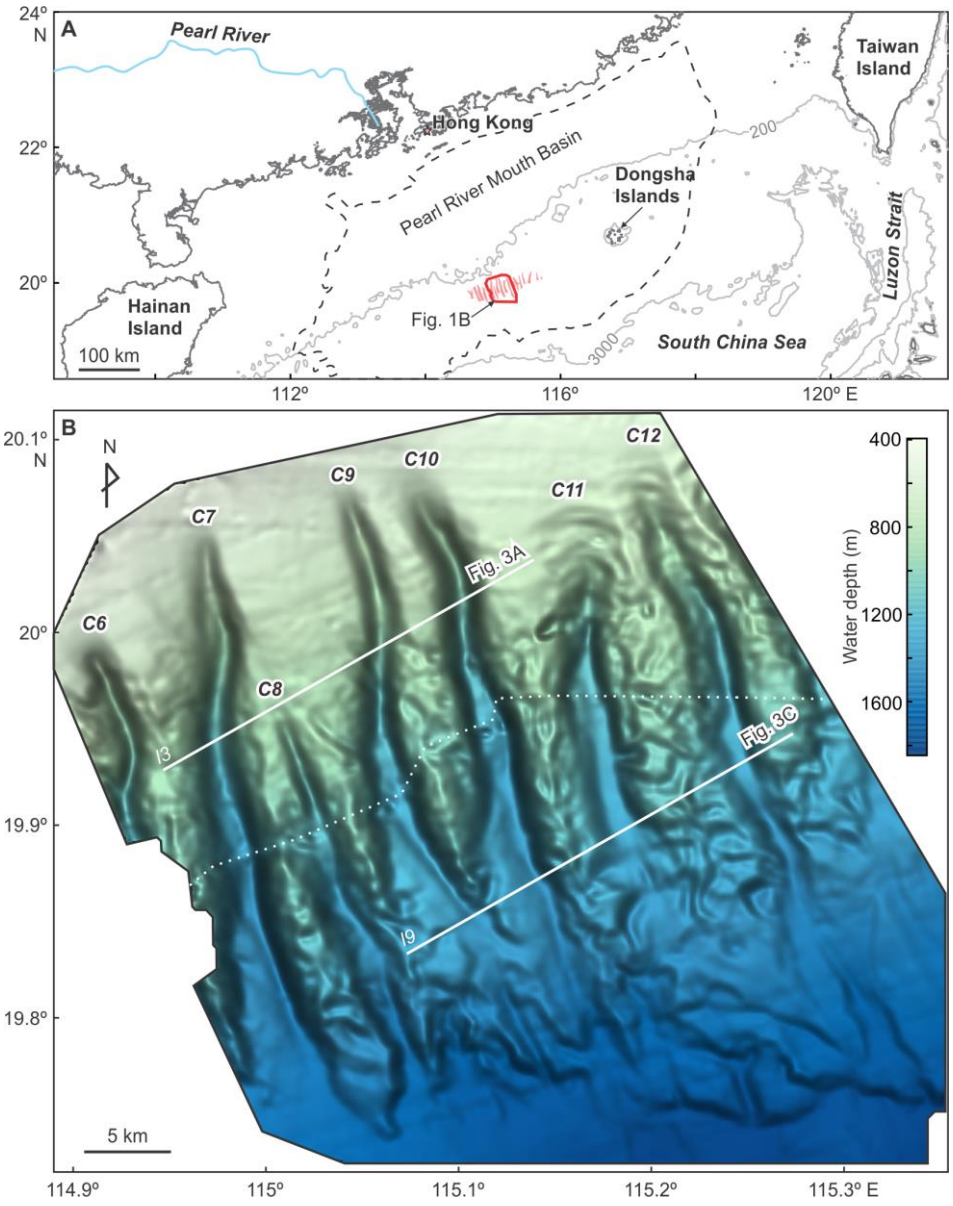

Fig. 1. Maps of the study area in the northern South China Sea. (A) Location map. The red outline shows the study area covered by the multibeam bathymetric surveys; The transparent red marks 19 submarine canyons documented by He et al. (2014); The dashed outline shows the boundary of the Pearl River Mouth basin. (B) Bathymetric features. The map contours and colors indicate bathymetry. The white lines mark the locations of the seismic profiles shown in Fig. 3. The white dotted line represents the boundary of 2004 (upper canyon reaches) and 2005 (lower canyon reaches) surveys. The white texts show names of seismic profiles. This map is based on the multibeam bathymetric survey data collected in 2004 and 2005.

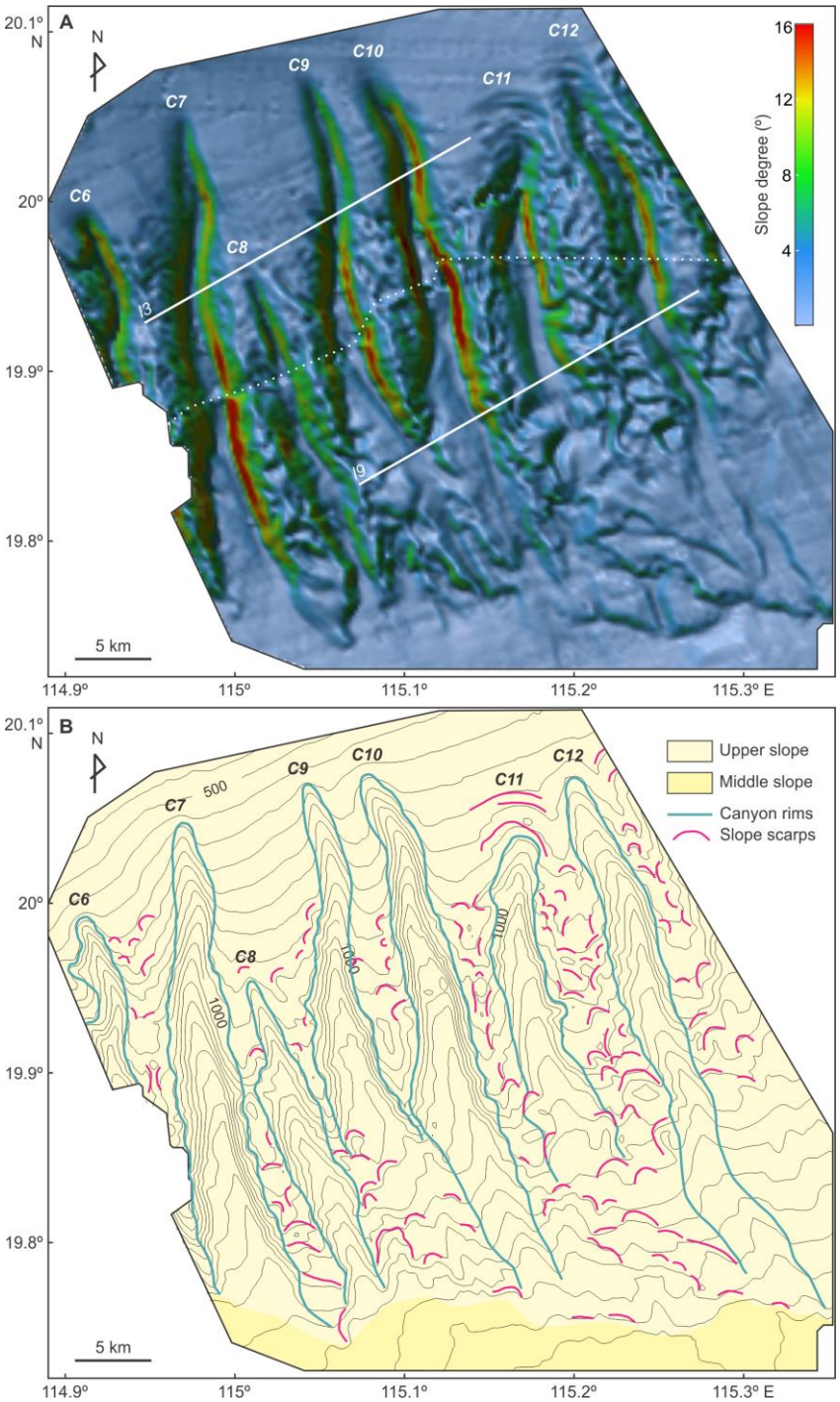

Fig. 2. Morphologic maps of the study area, based on the 2005 bathymetric survey. (A) Slope gradient map. White lines mark two seismic profiles used in this study. (B) Morphosedimentary interpretation. Canyon rims are defined by place of maximum slope change. The white dotted line represents the boundary of 2004 (upper canyon reaches) and 2005 (lower canyon reaches) surveys. The map contours indicate bathymetry (m). Contour interval = 50 m.

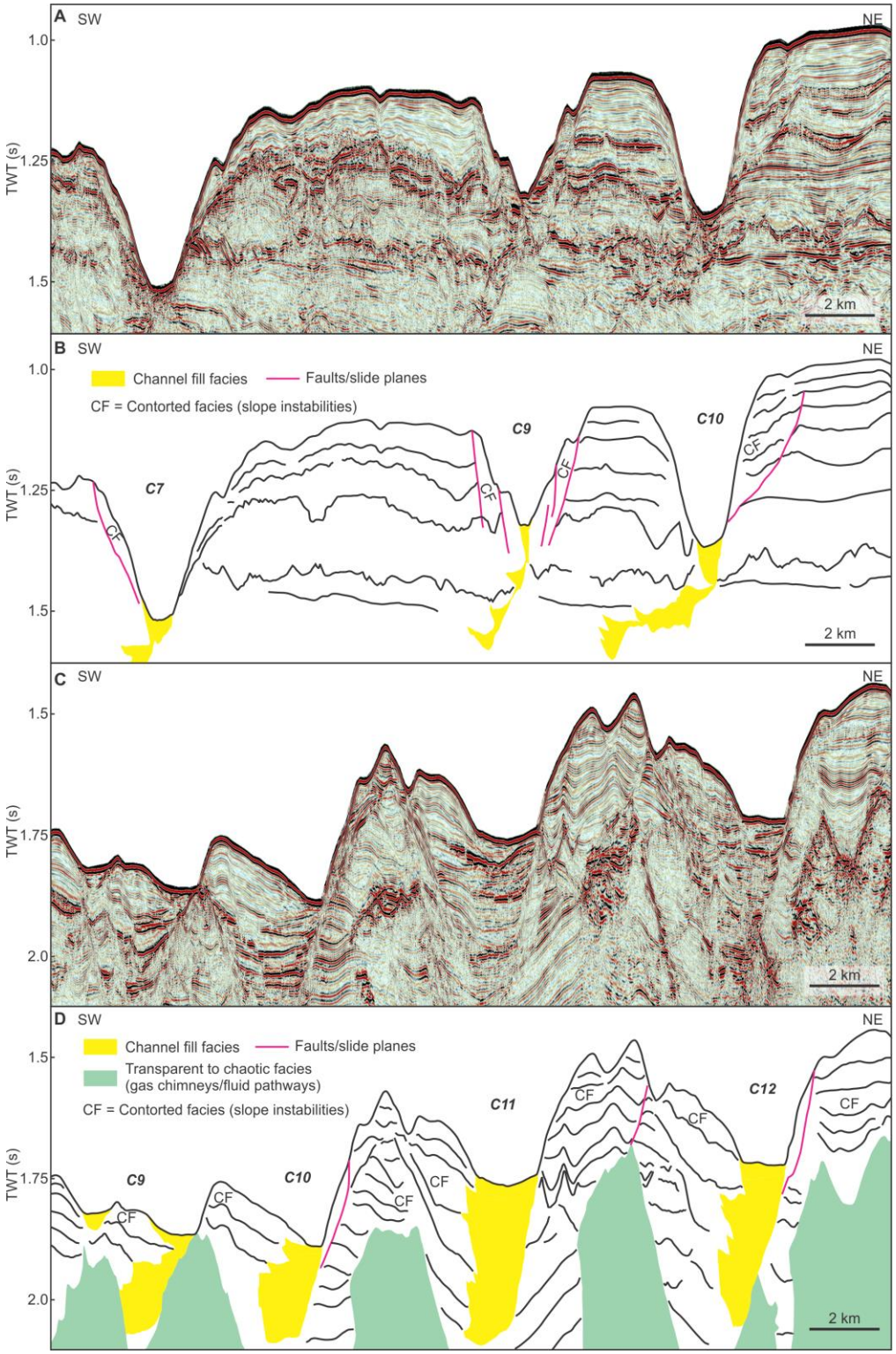

Fig. 3. Cross-canyon seismic reflection profiles and interpretive drawings. (A, B) Canyon segments in relatively shallow slope waters (approximately 800 m): C7, C9, and C10. (C, D) Canyon segments in deeper slope waters (approximately 1200 m): C9, C10, C11, and C12. Black lines in (B, D) represent high-amplitude reflections. Profile locations are shown in Fig. 1B.

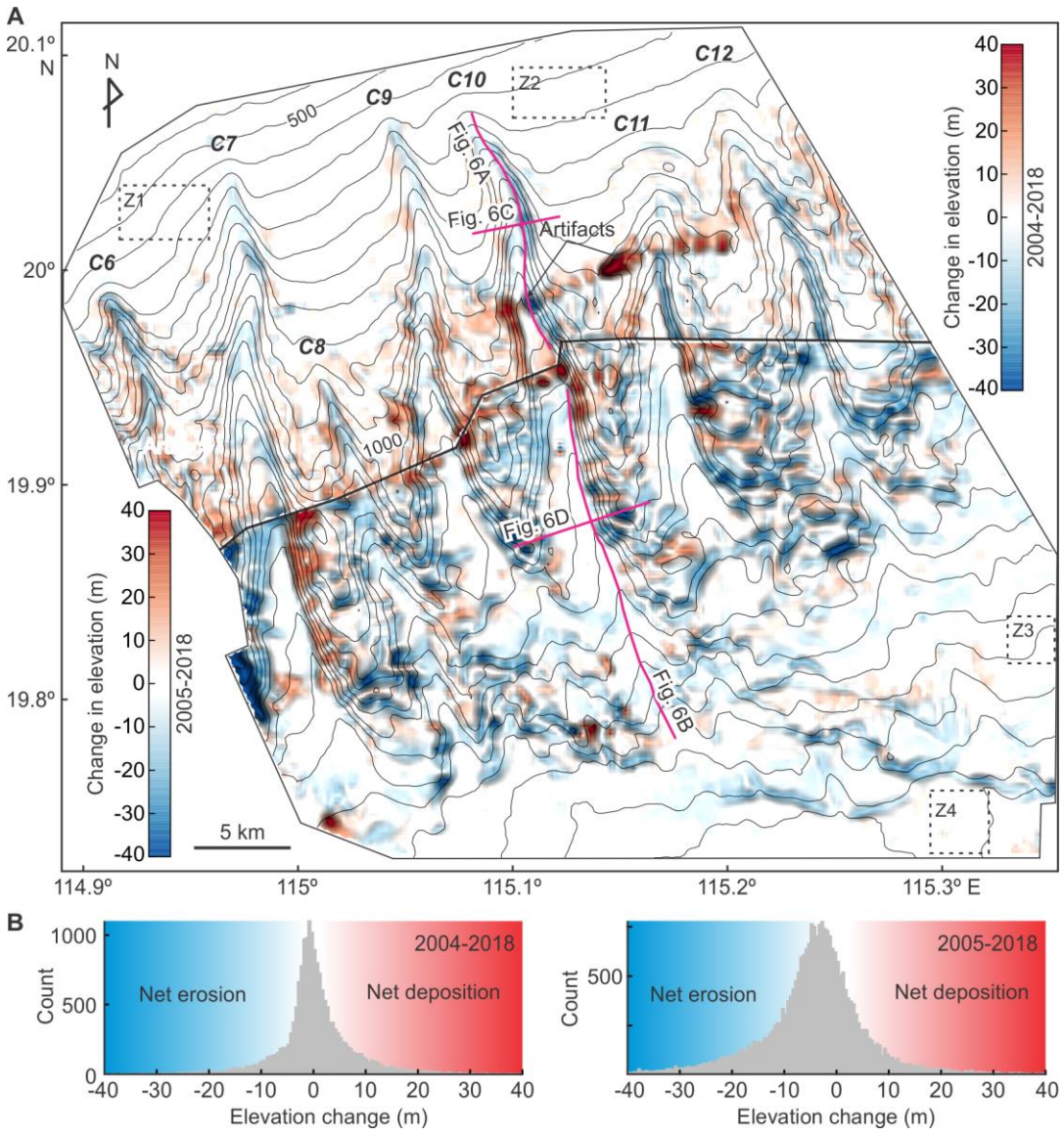

Fig. 4. Corrected and cropped change maps based on differences between the 2004 and 2018, 2005 and 2018 bathymetric surveys. (A) Elevation changes. (B) The frequency histograms of elevation differences in the entire 2004/2018 and 2005/2018 surveys. The thresholds of elevation differences between 2004 and 2008, and 2005 and 2008 are 1.5 m and 2.5 m, respectively. The carmine lines mark the location of vertical profiles in Fig. 6. Rectangles with dashed lines mark reference areas for estimation of accuracy and uncertainty of elevation differences. The black bold line represents the boundary of 2004 (upper canyon reaches) and 2005 (lower canyon reaches) surveys.

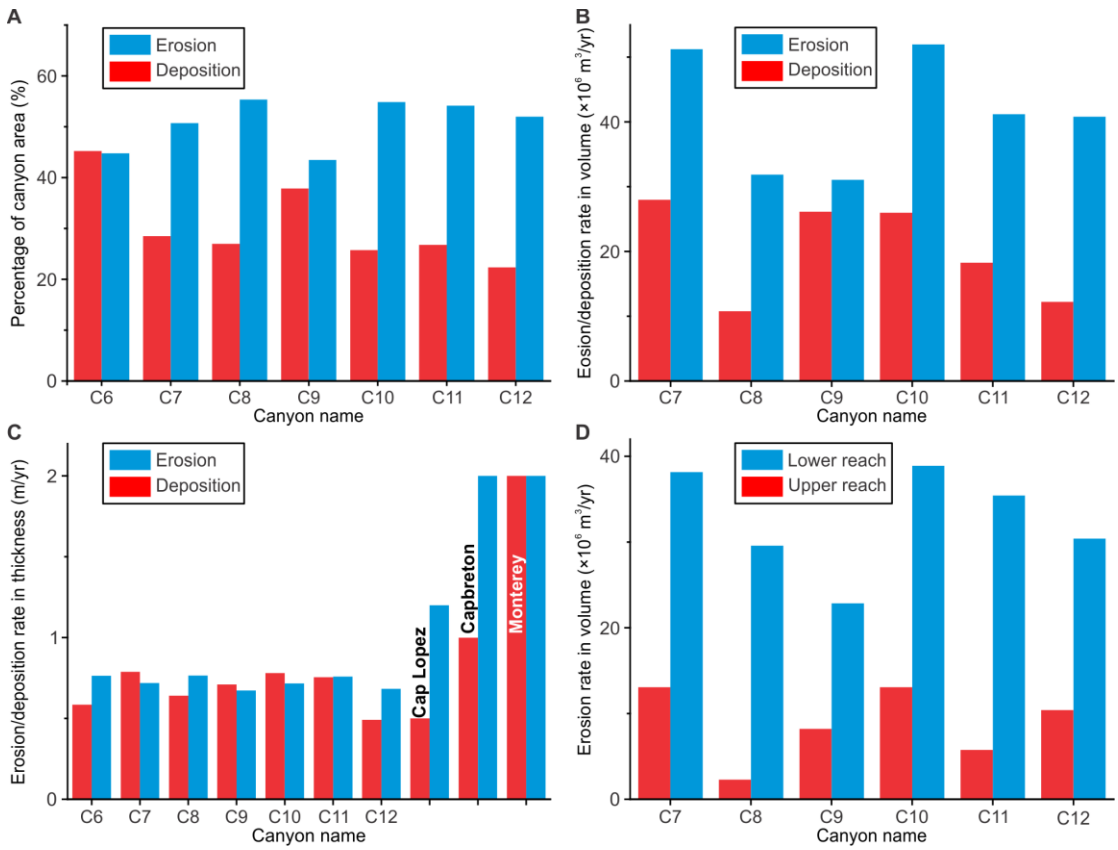

Fig. 5. Characteristics of erosional and depositional canyon change, on average of 2004–2018 and 2005–2018. (A) Areal extent of erosion and deposition, expressed as percentages of total area within each canyon. (B) Rates of erosion and deposition in volume. (C) Average rates of erosion and deposition in thickness. Recent average rates are also shown for shelf-incised canyons on other continental margins: Cap Lopez Canyon (Biscara et al., 2013), Capbreton Canyon (Mazières et al., 2014), and Monterey Canyon (Smith et al., 2005). (D) Erosion rates in volume in the upper (2004–2018) and lower (2005–2018) canyon reaches.

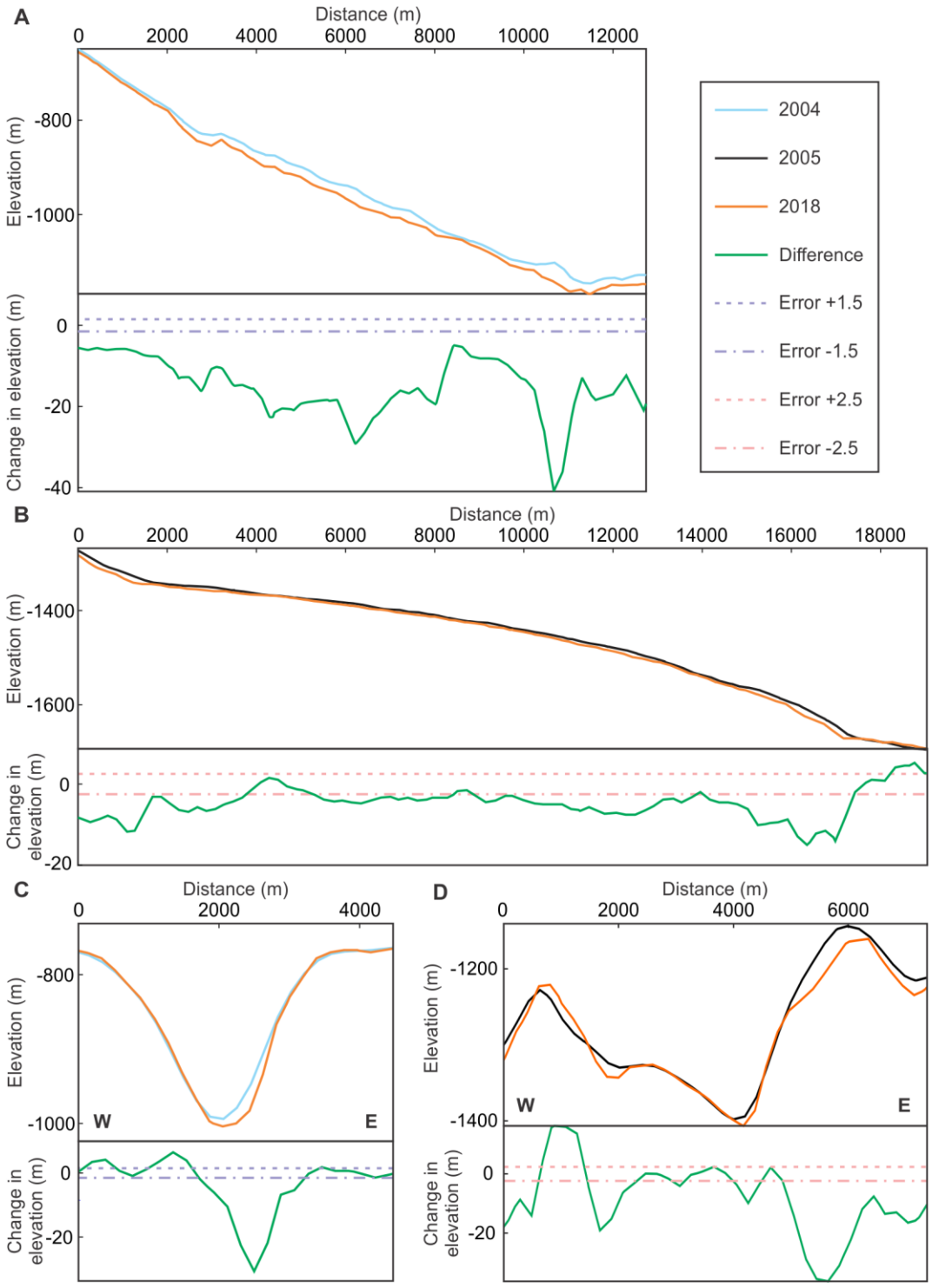

Fig. 6. Vertical profiles of elevation differences downslope (A, B) and cross-slope (C, D). Profile locations are shown in Fig. 4.

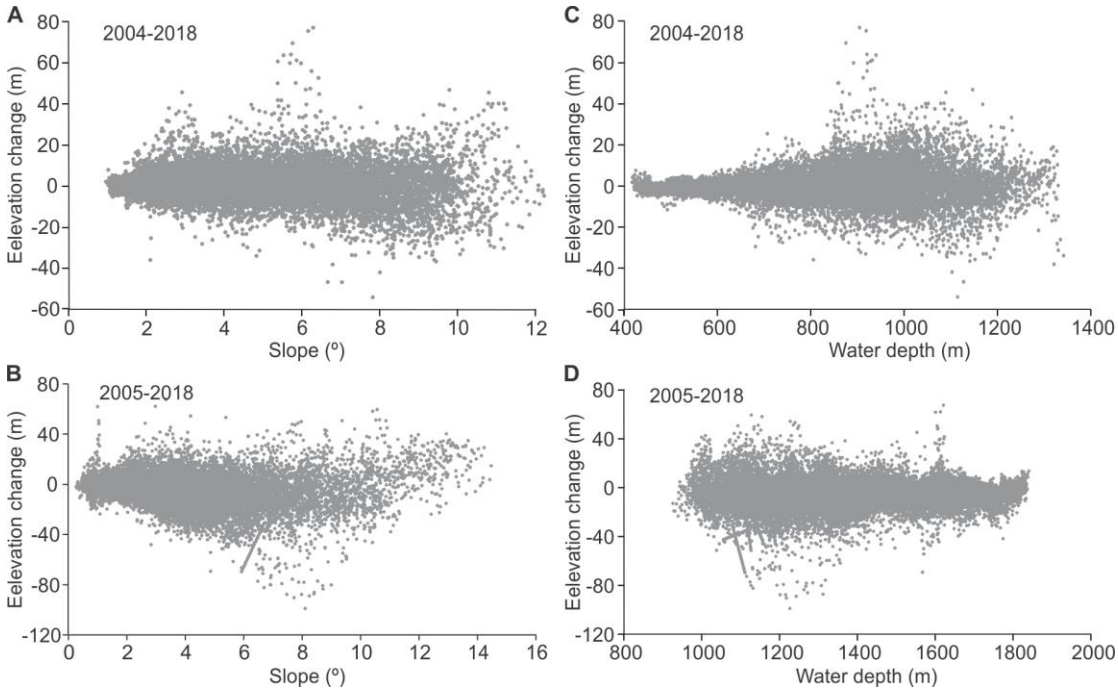

Fig. 7. Plots of slope vs elevation differences (A, B) and water depth vs elevation differences (C, D).

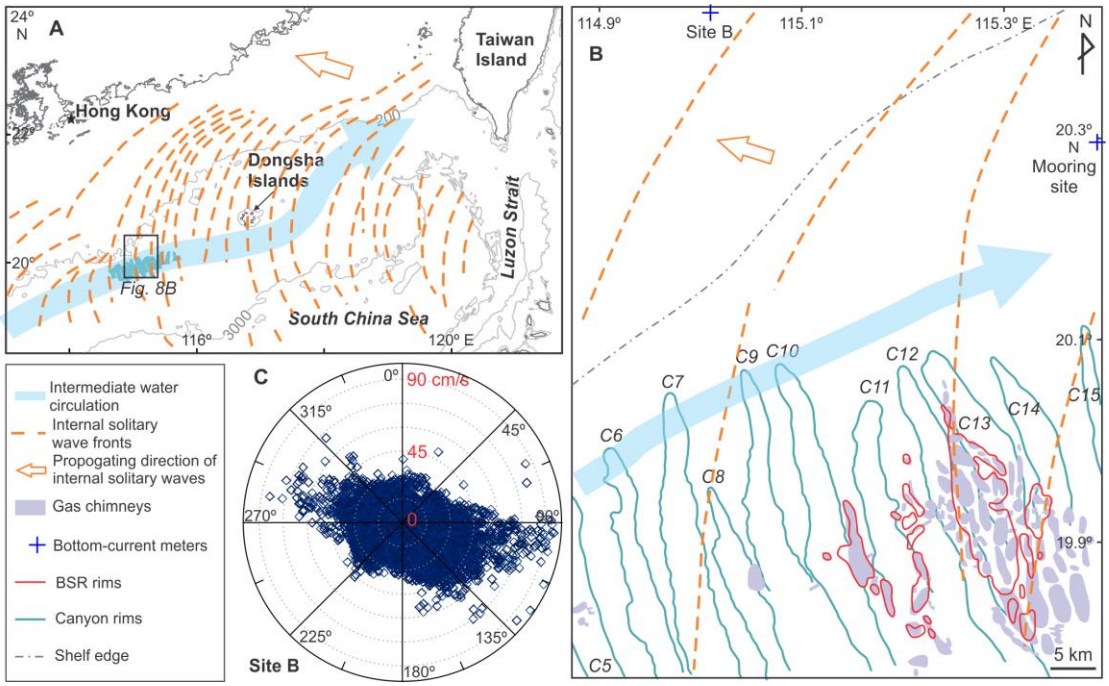

Fig. 8. Sketch illustrating oceanographic setting (A), sedimentary processes of the slope-confined canyons of the study area (B), and near-bed current-speed observation in the shelf at water depths of 175 m (C) that is modified from Ma et al. (2016). Internal solitary waves are responsible for erosion of upper canyon reaches and canyon migration. Activity of gas hydrates cause erosion of lower canyon reaches. Mapping of the internal solitary wave front is based on Wang et al. (2011). The mapping of the intermediate water circulation is based on Wang and Li (2009). The locations of the shelf-edge rims are based on Zhu et al. (2010), Zhou et al. (2015), and Wang et al. (2017). The bottom-simulator reflector (BSR) rim locations are from Chen et al. (2016). The mapping of the gas chimneys is based on the seismic profile shown in Fig. 3C and on Chen et al. (2016). The two near-bed current meters are described in Ma et al. (2016).